A novel biomechanical model of the mouse forelimb predicts muscle activity in optimal control simulations of reaching movements

Jesse I. Gilmer[1], Susan Coltman[5], Geraldine C. Velasco[2], John R. Hutchinson[4], Daniel Huber[2], Abigail L. Person[3], and Mazen Al Borno[1]

1. University of Colorado Denver | Anschutz Medical Campus, Department of Computer Science and Engineering, Computational Bioscience Program
2. University of Geneva, Department of Basic Neuroscience
3. University of Colorado Denver | Anschutz Medical Campus, Department of Physiology and Biophysics
4. Royal Veterinary College, Department of Comparative Biomedical Sciences
5. The Pennsylvania State University, Department of Kinesiology

ABSTRACT

Mice are key model organisms in genetics, neuroscience and motor systems physiology. Fine motor control tasks performed by mice have become widely used in assaying neural and biophysical motor system mechanisms, including lever or joystick manipulation, and reach-to-grasp tasks (Becker et al., 2019; Bollu et al., 2019; Conner at al., 2021). Although fine motor tasks provide useful insights into behaviors which require complex multi-joint motor control, there is no previously developed physiological biomechanical model of the adult mouse forelimb available for estimating kinematics (including joint angles, joint velocities, fiber lengths and fiber velocities) nor muscle activity or kinetics (including forces and moments) during these behaviors. Here we have developed a musculoskeletal model based on high-resolution imaging and reconstruction of the mouse forelimb that includes muscles spanning the neck, trunk, shoulder, and limbs using anatomical data. Physics-based optimal control simulations of the forelimb model were used to estimate *in vivo* muscle activity present when constrained to the tracked kinematics during mouse reaching movements. The activity of a subset of muscles was recorded via electromyography and used as the ground truth to assess the accuracy of the muscle patterning in simulation. We found that the synthesized muscle patterning in the forelimb model had a strong resemblance to empirical muscle patterning, suggesting that our model has utility in providing a realistic set of estimated muscle excitations over time when provided with a kinematic template. The strength of the resemblance between empirical muscle activity and optimal control predictions increases as mice performance improves throughout learning of the reaching task. Our computational tools are available as open-source in the OpenSim physics and modeling platform (Seth et al., 2018). Our model can enhance research into limb control across broad research topics and can inform analyses of motor learning, muscle synergies, neural patterning, and behavioral research that would otherwise be inaccessible.

INTRODUCTION

Mice are ubiquitous model organisms across many fields of biological research, including genetics, neuroscience and physiology. They provide access to a wide array of disease models, advanced molecular interrogation techniques, ease of husbandry through short gestation cycles, and the cost of raising and housing mice is relatively inexpensive. In addition to these factors, mice are often used in behavioral studies, including those that assay fine motor control. Mice can perform tasks like manipulandum control (Bollu et al., 2019), dexterous reach (Becker et al., 2020), and can learn complex behaviors with training (Burgess et al. 2017, Serradj et al., 2023, Sauerbrei et al., 2020, Galinanes et al., 2018, Conner at al., 2021). However, despite the utility of mice as a model organism in motor learning, there are no high-resolution reconstructions of the adult mouse forelimb, nor are there any physiological biomechanical models of their forelimbs that incorporate fully developed muscle morphology. Biomechanical models are useful for motor systems and neuromechanics researchers to provide detailed insights into muscle activity and limb kinematics (e.g., fiber length and velocities) that would otherwise be difficult or impossible to access through empirical observations. Experimentally measuring muscle activity is challenging due to the size of the mouse and the large number of muscles in the body. State-of-the-art methods can only measure the activity of 3-4 muscles in the 25+ muscles in the forelimb (Zia et al., 2020). Therefore, the construction and evaluation of a model of the mouse forelimb would be a valuable tool for researchers studying dexterous behaviors in mice.

The only currently available mouse forelimb model, developed recently in a full-body mouse model (Ramalingasetty et al., 21), was based on mouse embryo data (Delaurier et al., 2008), which also lacked many of the large muscles originating from the scapula, and on educated guesses. Ramalingasetty et al. noted that modeling the mouse forelimb is more challenging than the hindlimb, due to the lack of published biomechanical data, and improving their forelimb model was identified as a remaining challenge for future work. Reference books on limb anatomy present two-dimensional (2D) illustrations of the limb musculature (Hebel 1986), but it is challenging to extract accurate locations of the attachment points and the three-dimensional (3D) tissue paths from these references (Delaurier et al., 2008). By using large-scale light sheet microcopy data, we were able to more accurately identify the muscle attachment sites and muscle paths than by working with mouse and rat atlas data. Additionally, computing these quantities directly from dissections is challenging because of the size of the forelimb muscles, whose tendon insertion points are separated by as little as tens of microns. The attachment points have been shown to be the most important factor in estimating how effective a muscle is in producing a joint rotation or moment (Charles et al., 2016).

The study by Charles et al. has produced a detailed description of muscle anatomy integrated into a hindlimb biomechanical model. We sought to build on this work to create a forelimb model. We started by scanning and recreating the forelimbs of two adult mice. Muscles with insertions onto the humerus span most of the mouse's trunk and spine, necessitating imaging of much of the mouse body. We limited our reconstruction to muscles that had insertions onto the humerus, radius, and ulna, as reconstruction of muscles with insertions onto the scapula and those that inserted onto the hand was infeasible given the resolution of imaging performed. Once the muscles had been traced and reconstructed, they were used to set the musculoskeletal geometry of the biomechanical model, that is, the attachments points of the muscles on the bones and their lines of action. We used published results on mouse forelimb muscle architecture to set the muscle parameters in our model (Mathewson et al., 2012). The resulting model has 21 muscles and 5 bones (along with a composite hand body segment), with the scapula and clavicle serving as fixed position bodies. The model has four degrees-of-freedom: shoulder elevation, extension, and rotation, as well as elbow flexion. The model is also capable of wrist flexion and rotation, but these degrees-of-freedom were fixed during our simulations. We used the OpenSim modeling and physics simulation environment to develop the forelimb model (Delp et al. 2007, Kewley et al. 2024). We have also written custom code to convert the model for the MuJoCo physics simulation environment (Todorov et al. 2012).

To evaluate the utility of the model, we sought to replicate physiological kinematics and predict simultaneously recorded muscle activity. We used a dataset of thousands of reaches from three mice who had their kinematics and a subset of their muscle activity recorded during reaching movements. The empirical kinematics were used as constraints on the synthesized kinematics with optimal control. The

empirical muscle activity was used as a ground truth for comparison against the optimal control predictions (i.e., the synthesized muscle activity). The muscles recorded experimentally in the dataset were the biceps, triceps long head and triceps lateral head.

Reaching movements in mice, rats, and primates are widely studied in systems neuroscience to study healthy and injured motor networks (Fleischer et al., 2023; Khanna et al., 2021; Yang et al., 2023). However, reaching movements lack endpoint accuracy in patients with cerebellar disease (Bonnefoi-Kyriacou et al., 2018), exhibit abnormal muscle coordination patterns after stroke (Cheung et al., 2012) and have impaired kinematics in Parkinson's disease (Vissani et al., 2021). The mouse is an ideal model system for motor control research because of relatively easy access to neural, behavior and anatomical data, as well as to advanced molecular interrogation techniques for perturbation studies (Deisseroth et al., 2006). Building on a large body of prior work in primates, several research groups are conducting foundational studies on mouse reaching (Becker et al., 2020; Yang et al., 2022; Wagner et al., 2021; Conner et al., 2021; Galilanes et al., 2018), which are evolutionarily conserved (Iwaniuk 2000). Reaching movements are the focus of the model evaluation experiments in this study; however, the model could be used to simulate other forelimb movements.

There is an infinite number of possible muscle coordination patterns that are consistent with kinematics (Harris & Wolpert 1998). Optimal control chooses the muscle excitation pattern that achieves task constraints, while minimizing a proxy for effort or energy (e.g., the sum of muscle activations squared) and possibly other terms (Al Borno et al., 2020). We apply optimal control to predict an energetically efficient muscle activity pattern that achieves the reaching kinematics task. We focused this study on the ballistic phase of the reach and have not studied the grasping phase. To simplify the problem, we have not included the muscles that control the wrist and fingers in the biomechanical model and kept these degrees-of-freedom locked. However, we have provided the 3D reconstruction of some of these muscles in supplementary materials. We are not aware of any prior work that compared predicted muscle activity with empirical muscle activity for three-dimensional reaching movements (in humans or other species).

Optimal control-based simulations using the model were able to recreate reach kinematics accurately using synthesized muscle excitations. The muscle patterning produced when constrained to replicate experimental reach kinematics had a strong resemblance to empirical electromyography (EMG) data. The model performed best when estimating the mean EMG rather than on a reach-per-reach basis because of the high physiological variance in the muscle patterning employed in mice. Mean EMG predictions were within 1 standard deviation of mean experimental EMG in most reaches and produced lower error than time-shuffled EMG. These results suggest that our model can replicate realistic reach kinematics and muscle activity. Our analysis reveals that the optimal control solutions are closer to the empirical solutions (i.e., the patterns employed by real mice) as reaching performance improves throughout learning. In other words, mice employ muscle patterning solutions that more closely resemble optimal control solutions as they become more skilled at the task. More broadly, this model should provide insight into forelimb behaviors that would otherwise be inaccessible by experimental means, and we hope that access to a robust description of the forelimb's kinematics, forces, and muscle activity will advance understanding of mouse behavior. Our computational tools are available as open-source for researchers interested in analyzing muscle activity during mouse forelimb movements.

METHODS

Anatomical high-resolution imaging

Accurate prediction of muscle activity during movements is predicated on a sufficient description of the underlying anatomy and physiology. To produce a model that was suited for prediction tasks, we first sought to gather anatomical data to inform the model. We obtained 3D scans of mouse forelimbs and trunk musculature through large scale light sheet microscopy imaging of two wildtype female mice (9 weeks old). The dataset contains imaging that captured the left distal shoulder and proximal forelimb (Mouse A), the right distal forelimb and paw (Mouse A), and both forelimbs, shoulders, and trunk (Mouse B). Only the left shoulder, trunk, and proximal forelimb were reconstructed in Mouse B.

Mouse and tissue preparation

Mice were euthanized via subcutaneous injection of pentobarbital and prepared for imaging though fixation with a transcardial injection of 4% paraformaldehyde (PFA) and 0.01% heparin. The vascular system was washed with a saline solution before and after perfusion with PFA, then washed overnight in phosphate-buffered saline (PBS) and 0.01 heparin. Mouse A was dissected, with skin removed and forearm separated axially to the vertebral column.

Imaging subjects were prepared using the iDISCO+ tissue clearing methodology (Habart et al., 2023). The tissue was introduced to a gradually increasing concentration of methanol, starting with 20% and increasing by 20% every hour. The clearing chamber was maintained at room temperature. After 5 hours of exposure to methanol, the tissue was chilled at 4° C overnight and then bathed in 66% dichloromethane (DCM) and 33% methanol for 24 hours. The tissue was then bathed in 100% methanol for 2 hours before being chilled for 1 hour and then transferred into 5% hydrogen peroxide in methanol for 48 hours. Finally, tissue was rehydrated through 1 hour immersion in 80%/60%/40%/20% methanol for one hour per 20% decrement, then transferred to 1x PBS for 24 hours, followed by immersion in a 100ml PBS 10x and 2 ml TritonX-100 solution that was filled to 1L with distillate water.

After clearing was completed, the tissue was prepared for immunostaining without antibodies via incubation a permeabilization solution (500 mL) consisting of 400 mL PTx.2, 11.5 g glycine, and 100 mL dimethylsulfoxide (DMSO). The tissue was bathed in solution for 4 days, then transferred to a blocking solution of 42 mL PTx.2, 3 mL donkey serum, and 5 mL DMSO for 3 days. Finally, tissue was washed with 100 mL PBS 10X, 2 mL Tween-20, 1 mL of 10mg/mL heparin, and filled to 1L with distillate water. The tissue was then re-cleared through preparation in 20%/40%/60%/80%/100% methanol in 1-hour steps, then bathed in 100% methanol overnight. Afterwards, the tissue was bathed in 66% DCM and 33% methanol for 4 hours, then in 100% DCM for 15 minutes twice in succession.

Imaging parameters

Dissected mouse limbs were arranged in a prone position prior to imaging. Scans were taken with 8.23 um per pixel scans at 8x zoom, with 5 um steps in the z-plane. Imaging was performed using mesoSPIM (Voigt, et al., 2019). Immunostaining was captured in the green channel (488 nm laser) and was imaged using mode tiling wizard with an offset by 75% and a filter set to 530/43. Mouse A's forearms were dissected and imaged in their entirety. Mouse B was imaged from the base of the skull through the joint of the femur and tibia and the entirety of the depth of the sample.

Anatomical segmentation and reconstruction

The basis for this study was to obtain physiological morphology data from the mouse forelimb to inform the development of a musculoskeletal model for usage in optimal control-based simulations. We found that muscle density and striation was a sufficient marker of muscles to identify them with light sheet microscopy, which were enhanced through immunostaining without antibodies (see **Methods: Mouse and tissue preparation**). We used the raw imaging of the mouse anatomy and segmented individual muscles into 3D shape objects using 3D Slicer (Federov et al., 2012) (Fig. 1A). We also segmented the forelimb bones to obtain landmarks and geometries for use in the model, such as the deltoid tuberosity of the humerus, which is a site of attachment for many shoulder muscles in the mouse. Because not every data set had complete

data for the entire forelimb, right and left anatomical datasets were combined through manual alignment in Blender (Blender D.T., 2022). We used anatomical landmarks on the humerus, ulna, and radius to align muscle reconstructions, as these bones were present in all three imagining datasets. The reconstructions were scaled according to the radius of the bones and confirmed visually by examining the degree of overlap between reconstructions.

Development of a biomechanical model of the mouse forelimb

With a detailed set of reconstructions, we next sought to leverage anatomical descriptions to construct a biomechanical model in OpenSim, a widely-used physics-based modeling and simulation environment used to study movements of humans and other species. The anatomical model was assembled using OpenSim Creator (Kewley et al., 2024). We have also converted the model in MuJoCo (Todorov et al. 2012), which produces faster (but less physiologically accurate) simulations that are more amenable for deep reinforcement learning applications. Although the model is available in MuJoCo, the computational tools for optimal control are based in OpenSim; therefore, MuJoCo users will need to develop their own code to produce the simulations with the model. Each individual muscle was measured and a combination of parameters derived from optical measurement, and from previous parameters in Mathewson et al., 2012 and Charles et al., 2016, were used to derive the biophysical properties of the modelled muscles. We used De Groote-Fregly (De Groote et al., 2016) Hill-type muscles within the model, and opted to ignore complex tendon dynamics (i.e., using rigid tendons with no force-length/velocity properties), both to facilitate the production of a functional model and because we did not have access to sufficient data regarding tendon physiology purely from imaging data. The model is likely to improve from a more detailed dissection and biophysical tests, but these assays were beyond the scope of this project.

The musculotendon units in the forelimb were modeled by the common Hill-type muscle (Uchida & Delp 2021), which is parametrized by four parameters (maximum isometric force, optimal fiber length, tendon slack length and pennation angle). All these parameters, except for tendon slack length, were determined experimentally in the muscle dissection study of Mathewson et al., 2012 and through interpolation from known values when a muscle was not described in prior literature. The tendon slack length parameter represents the length where a tendon develops passive elastic force (Uchida & Delp 2021). This parameter cannot be measured experimentally and was set using the optimization procedure of Buchanan et al., 2004, as is commonly performed in the field (Charles et al., 2016), assuming that muscle fibers remain within 0.5 to 1.5 times optimal fiber length throughout the joint's range of motion, which were estimated from both anatomical constraints and video of mouse behavior. Based on the muscle paths from the digital segmentation, we used wrapping surfaces, which are geometric objects in OpenSim, to constrain the muscles to have realistic paths of action. This is necessary for the model to produce realistic moment arms (Charles et al., 2016). We set other parameters in the muscles such as the maximum contraction velocity, the activation time constants and the force-length curves scaled based on prior work on mouse physiology (Charles et al., 2016; see open-source model for details). We calculated the physiological cross-sectional area (PCSA) by the standard formula developed by Alexander & Vernon (1975), that is, muscle volume divided by fiber length. Muscle fiber pennation angle is entered separately in OpenSim models; thus not directly used in PCSA calculations. Bone volume was determined in reconstruction and was uniformly multiplied by a murine bone density scalar (.00425 kg/cm^2) determined from a literature search for empirical measures (Robbins et al. 2018) and prior models of the mouse (Charles et al., 2016), as well as estimations of the center-of-mass and inertia. A description of the model geometry is available in Table 1 and the muscle parameterization in Table 2.

Model scaling

Individual mice have variable limb dimensions that models must be altered to accommodate. We accomplished this by using the scale tool in OpenSim to automatically scale the mass, length, and muscle parameters of the model to fit the observed kinematic data originating from a particular mouse subject. We used DeepLabCut (Mathis et al., 2018) to estimate paw, elbow and shoulder markers from video. Our scripts adjusted the marker positions based on a 2D skeletal model with estimated limb lengths (derived from mean

inter-marker distances). These adjusted marker positions were then used to scale the OpenSim model to the mouse's proportions.

Mouse behavior

Evaluation of the model against a behavioral dataset with a known ground truth, both in terms of kinematics and muscle activity, is necessary to assay its utility. Mouse behavior was recorded from two cameras during reaching behaviors and then processed using the DeepLabCut 3D motion tracking software (Mathis et al., 2018). We collected data in a forelimb reaching task and recorded electromyography (EMG) from the biceps brachii, triceps long head, and triceps lateral head. The activity of three muscles were measured simultaneously with Myomatrix arrays (Zia et al., 2020). We estimated the elbow joint angle from the 3D markers. We used the average limb lengths to adjust the DeepLabCut paw, elbow and shoulder markers and ensure that the limb lengths remain constant throughout the video, which is necessary for accurate tracking by the model. Because our forelimb model only has rotational degrees-of-freedom on the shoulder, we could not capture the small translational movement occurring at the shoulder during head-fixed reaching. We subtracted the shoulder markers displacements from the elbow and paw markers to keep shoulder positional coordinates fixed in our simulations.

Processed EMG envelopes were normalized to the maximum contraction recording during the session. EMG is usually normalized to the maximum voluntary contractions in studies with human subjects (Kendall et al., 2005). We rectified the EMG signals and then filtered them with a bandpass and lowpass filter suite. We bandpassed the signal from 5 to 500 Hz, rectified the signal, then low-passed further with a cutoff of 10 Hz. Additionally, we normalized the filtered EMG signals with a z-score measure. Each muscle was recorded through 4 leads, but only the qualitatively determined cleanest lead per muscle was used for this study.

Mice were kept at 80% body weight during their training and testing periods, and mice were head-fixed to a behavioral platform while reaching for small pellets (Figs. 1D, 2A). Mouse EMG was recorded from session one, when the mouse was completely naïve, and training progressed indefinitely until expertise was reached. The mice in this dataset ranged from having 11 to 26 total sessions, up to 1 hour per session. The mice used for this study achieved an initial successful reach on a range of sessions spanning 2-5 days.

Selection of reaches for simulation

Our dataset spanned the entirety of reach training for 3 mice, and because of the progression of learning, there was natural variance in kinematics performed. We opted to select only from 'expert' mice and to use baseline EMG datasets that were derived from similar reaching kinematics. We grouped reaches using the 2-norm metric on 3D paw kinematics to assess similarity, and then selected two sets of 10 reaches per mice, with each set having a different kinematic profile (i.e., qualitatively different paw trajectories). We enforced expertise by selecting reaches that occurred only after the initial 4 sessions of learning, which was a typical epoch for mice to reach moderate success in reaching. We also compared the optimal control predictions between the early and late sessions of learning. Early sessions were selected from the 3 mice discussed above, with an additional mouse who did not achieve expert status included. 10 reaches were selected from each mouse for the early dataset. Early sessions were restricted to the first 3 sessions of learned reaching.

Optimal control

To demonstrate the ability of the model to synthesize physiological movements, kinematics were recorded using DeepLabCut (Mathis et al., 2018). These provided 3D coordinates of the paw and elbow during head-fixed reaching movements. Optimization was conducted with direct collocation in Moco (Dembia et al., 2020) as it is well-suited for simulations that track experimental data ("inverse simulations"; e.g., Bishop et al., 2021). Direct collocation enforces the equations-of-motion and physiological relationships as constraints in a nonlinear optimization problem which solves for the states of the musculoskeletal system and the muscle activity over the duration of the simulation. The optimization's objective is to minimize a cost function of two terms: one term that is a proxy for effort (i.e., the sum of muscle activations squared)

and one term that represents the tracking cost (i.e., the deviation between the synthesized and the experimental kinematics). The cost function equation is:

$$E = wT_{paw} + wT_{elbow} + \sum_i a_i^2$$

Here, T_{paw} is the 2-norm squared difference between model and experimental 3D paw coordinates. The experimental coordinates comprised of 100 timepoints during the ballistic phase of reaching. The same holds for T_{elbow}, which is derived from tracking of the mouse elbow position. Term a_i denotes the activation of muscle i in the model and w is a scalar weight set to 10^9 .We optimized over 2500 iterations and 100 mesh points. The simulation was also constrained to start and end with the joint angles derived during the scaling of model. The optimization would end early if a convergence tolerance of $1e^{-7}$ was reached. The optimization typically ran for 10 minutes on a computer with specifications listed in supplemental Table 1.

The empirical muscle activity was not fitted or used by the optimization. Muscle activity is predicted based on optimality, task, physics and physiological constraints. We compared the predicted muscle activity with electromyography measurements on the triceps lateral head, triceps long head and biceps in 3 mice. We compared the activity of the recorded muscles to the muscle excitations produced by the model with the mean absolute error (MAE) metric at an optimal lag (in a range of –50 to +10 ms; we used a lag of 0 ms for Figure 3 and the late reach set in Figure 4; early reaches had an optimal lag of –50 ms in Figure 4). As a validation of the optimal control solutions, we compare the synthesized kinematics between the musculoskeletal model and a torque-based model without muscles, but with motors on the joints. We verified that the kinematics in muscle-based solutions closely recapitulated those in torque-based solutions, indicating that the optimization converged to adequate kinematic solutions (i.e. kinematic means were within a single standard deviation of the true kinematic mean across all dimensions, Figure 2: blue violin plots).

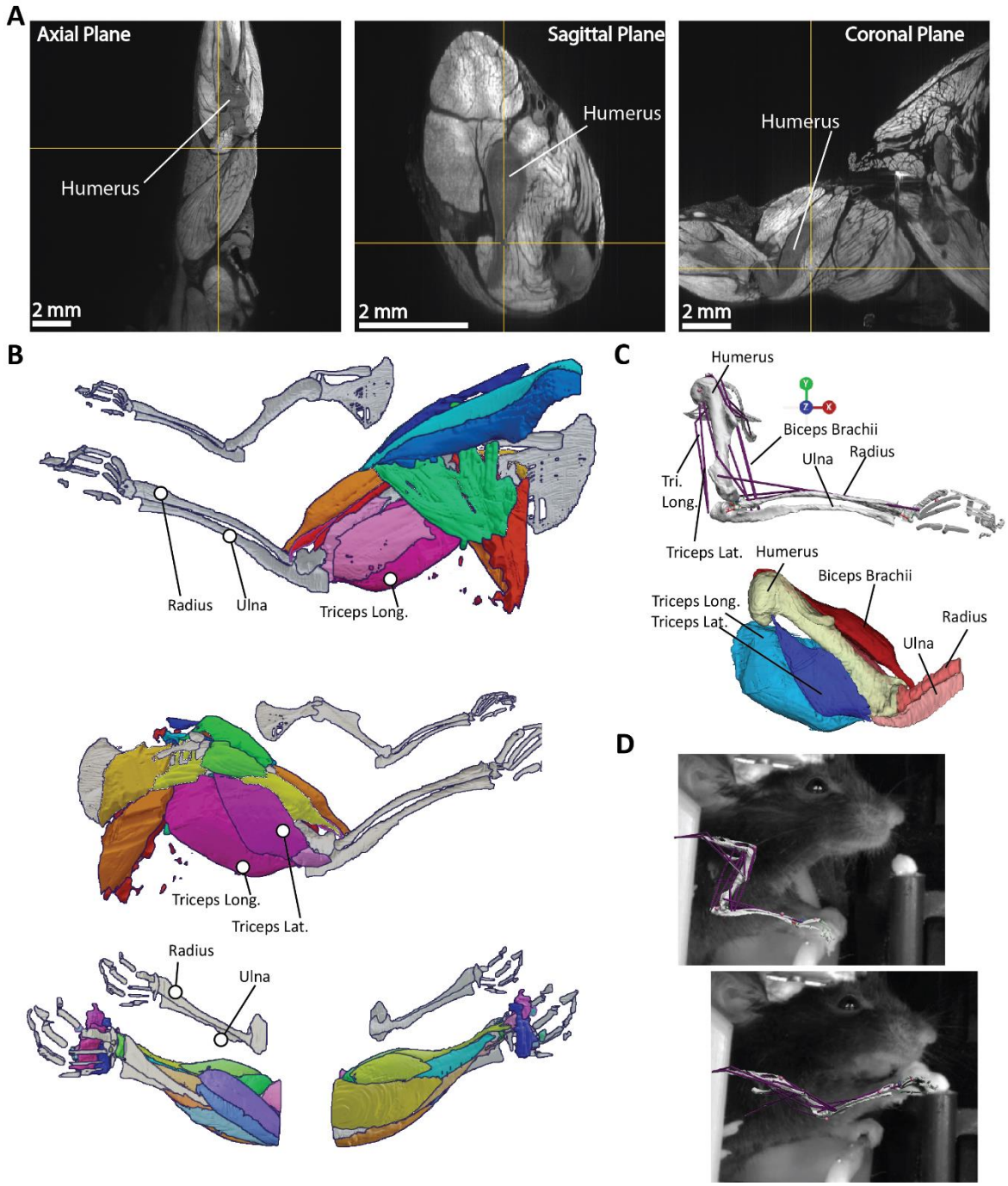

Figure 1. Anatomical reconstruction. A. Optical slices of the mouse forelimb in the axial, sagittal, and coronal planes. The mouse arm is oriented in the prone position. Labels added to highlight prominent muscles as an example of a reconstruction target. **B.** 3D projections of optical tracing results as a composite across mice. Upper panels show composite scan, while lower panels show the left hand of mouse A to highlight density of wrist-inserting muscles. 3D projections show morphology and attachment sites of muscles on bones that were used to create biophysical model. **C.** Biomechanical model (OpenSim) reconstruction developed from the 3D projections. **D.** Biomechanical model projection on video of mouse reaching.

RESULTS

Mouse forelimb musculoskeletal anatomy and biomechanical model construction

Table 1 and 2 provide data on the muscles segmented in this study, including their origins, insertions, and physiological properties which were derived from optical scans (Fig. 1A-C). Overall, we segmented over 21 muscles and 5 bones. The constructed biomechanical model has 21 muscles, 4 degrees-of-freedom (Fig. 1C) and was sufficient to describe ballistic reaching movements (Fig. 1D).

Kinematic Tracking

We tasked the physiological forelimb model to track recorded DeepLabCut-tracked kinematics using optimal control algorithms (see **Methods: Optimal control)**. Because there was natural variance in reaching movements and motor control, we opted to group 6 sets of 10 reaches by their kinematic similarity across time (see **Methods: Selection of reaches for simulation)**. We deliberately selected 6 sets of varying reaching kinematics to explore the ability of the model to predict varied motor behaviors. The model was scaled and then optimized with direct collocation (using OpenSim Moco, Dembia et al., 2021) to track the paw and elbow across the ballistic epoch of the reach (Figure 2). We were able to recreate limb kinematics with low error, with the majority of synthesized kinematics per timestep falling within 1 standard deviation of the empirical kinematic mean (Fig. 2C, blue violin plots; N = 60 reaches) across the x, y, and z dimensions of the paw and elbow trajectories.

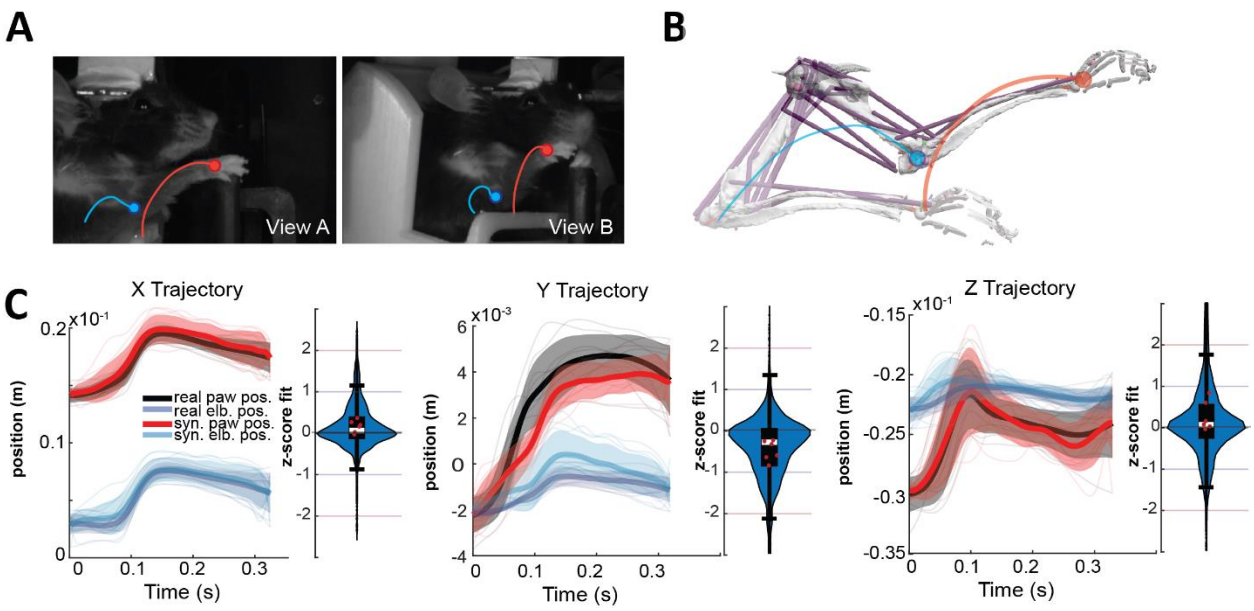

Figure 2. A. Example video with schematic elbow and paw marker trajectories. **B.** A biomechanical model with virtual markers on the elbow and paw. An optimal control problem is solved to minimize the difference between the virtual and empirical markers. **C.** Mean and standard deviation of 60 reaches for the empirical and synthesized marker trajectories. The z-score of the synthesized markers are largely within 1 standard deviation (see violin plots in blue), and the means per set of 10 reaches are all within 1 standard deviation (red dots). Black box plots denote median (white bar), 25 to 75th percentile distributions (black box), and 10th to 90th percentile distributions (short horizontal black lines).

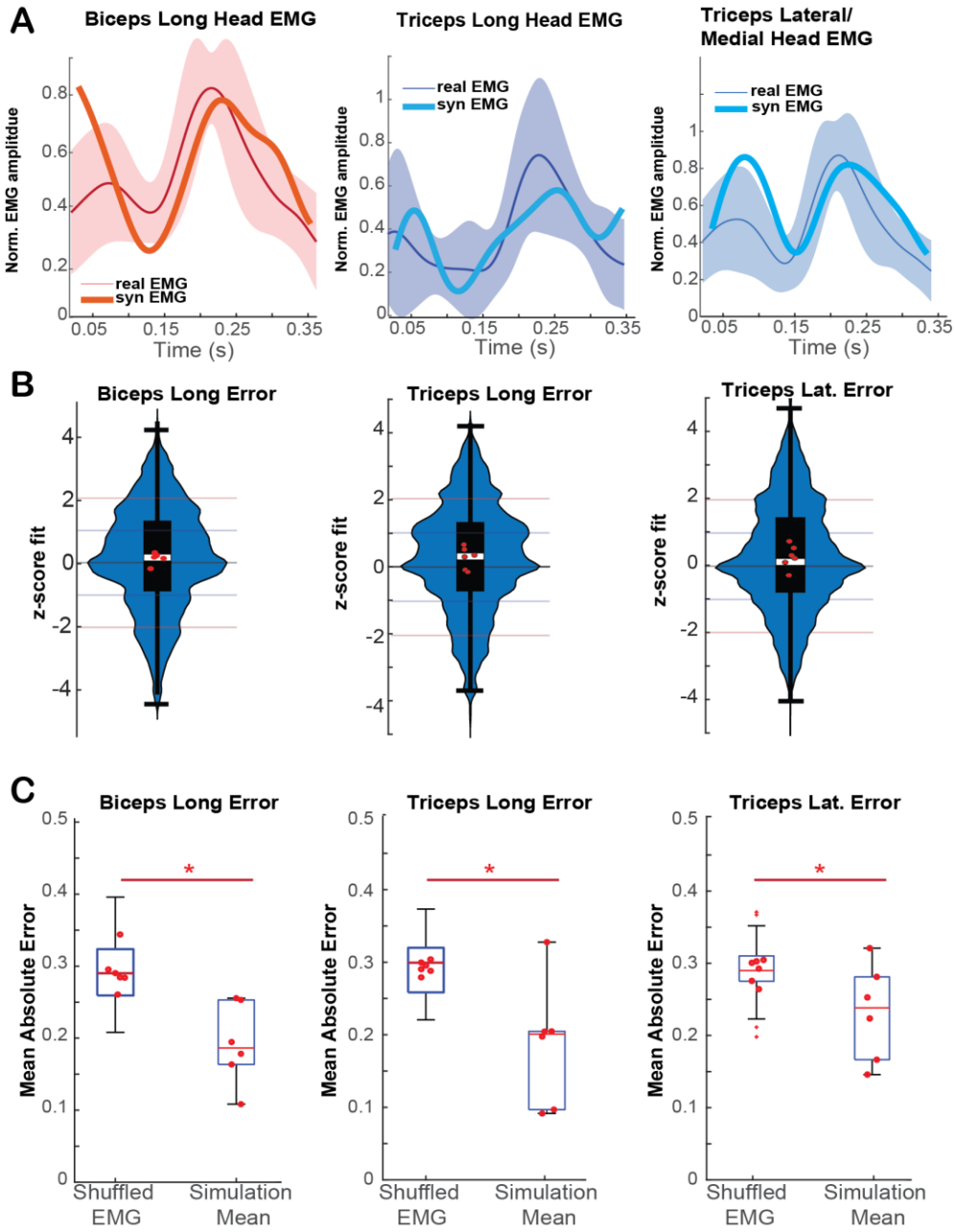

Figure 3. A. Comparisons of synthesized muscle excitations and experimental EMG activity. Curves show means and standard deviations (line and shaded region) of 10 reaches with similar experimental elbow and paw trajectories that were chosen from mouse behavior dataset. The mean synthesized excitations are shown in thick red for biceps long head, thick cyan for triceps long head, and thick blue for triceps medial head compared to the base lateral head activity. **B.** Violin plots including the entire dataset of 60 reaches. The mean synthesized muscle activity lies largely within 1 standard deviation of mean experimental muscle activity (red dots). On a reach-by-reach basis, the synthesized muscle activity lies largely within a z-score of 2 standard deviations (blue violin plots). Black box plots denote median z-deviation (white bar), 25 to 75th percentile distributions (black box), and 10th to 90th percentile distributions (horizontal black line). **C.** A comparison of mean absolute error between time-shuffled physiological EMG data and synthetic excitation means to the real mean of the tracked data. Synthetic excitation means have lower MAE than the time-shuffled data in all three muscles recorded (two-sided t-test, biceps p = 2.2e-6, triceps long head p = 1.4e-6, triceps lateral head p =4.8e-4. P-values were Holm-Bonferroni corrected for multiple comparisons). Black

box plots denote median (red horizonal bar), 25 to 75th percentile distributions (black box), and 10th to 90th percentile distributions (short horizontal black lines and stems).

Model muscle activity patterning for reaching movements

We tasked the model to synthesize muscle activity during reaching movements with optimal control. We experimentally recorded activity from the biceps, triceps lateral head, and triceps long head in 3 mice. We then synthesized muscle activity to recapitulate experimental kinematics with direct collocation using OpenSim Moco. As shown in the examples in Fig. 3A, we observe that the mean synthesized muscle activity closely resembles empirical muscle activity over the duration of the reach for all three muscles. We measure the performance of the model via the MAE of normalized ground truth EMG signals from model signals. The mean muscle excitations produced by the model were within a single standard deviation of the experimental EMG activity (Fig. 3B, red dots in violin plots; between 50-57 of the 60 reaches, depending on the mice and assayed muscle). On a reach-by-reach basis, the muscle excitations produced by the model across all time points were typically within two standard deviations of the experimental EMG activity. Paired reach-to-reach predictions were less accurate because mice were highly variable in their muscle patterning for the same kinematic profile (and some muscle patterns may be inefficient, more consistent with early learning or motor exploration, which would not be predicted as accurately by optimal control approaches). In Fig. 3C, we show that the mean model EMG predictions outperform the shuffled experimental EMG data (i.e., having the same distribution as the ground truth EMG; two-sided t-test, biceps p = 2.2e-6, triceps long head p = 1.4e-6, triceps lateral head p =4.8e-4.; P-values were Holm-Bonferroni corrected for multiple comparisons, N = 60 shuffled trials and 6 synthesized means).

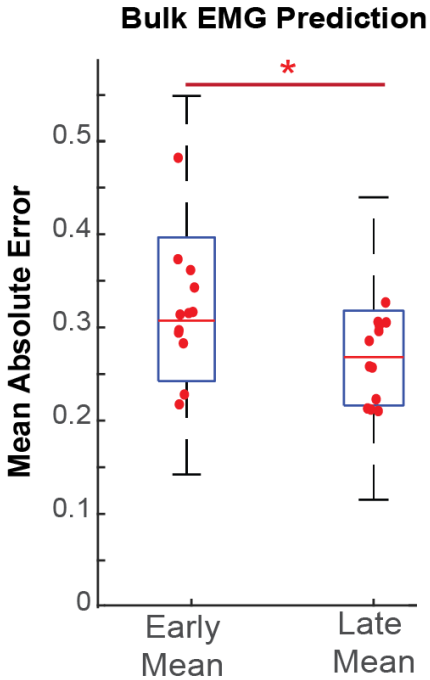

Figure 4. A comparison of the utility of the simulated muscle excitations in predicting trial-to-trial electromyography (EMG) during early or late training sessions (i.e. the first three sessions after the first successful reaches being *early* and sessions later than four sessions after the initial successful reach being *late*.) Late reaches, on bulk, have a significantly lower mean absolute error than early sessions (two-sided t-test, p = 3.5e-6, early N = 40, late N = 60) for predicting trial-to-trial EMG activity. Black box plots denote median (red horizonal bar), 25 to 75th percentile distributions (black box), and 10th to 90th percentile distributions (short horizontal black lines and stems).

Mouse motor learning and optimal control

The progression of reach kinematics and muscle patterning in mice learning a novel task is a relatively understudied phenomenon. We investigated the possibility that mice approach an optimal motor control solution during the progression of training by evaluating optimal control predictions during early and late sessions of training. In Fig. 3, we compared the optimal control predictions with reaches selected from expert mice (i.e., after at least 5 sessions of successful reaching). In Fig. 4, we compared how the optimal control predictions varied when the reaches were chosen in the early (i.e., in the first 3 sessions after the first successful reach to pellet) or late stages of learning. We found that mice tended to use muscle excitation patterns that converged more closely to those derived from optimal control in the later stages of learning. These results were significant when pooling the data across all recorded EMG channels but not on individual channels, likely because of our small sample size (early N = 4, late N = 6 for means comparisons, early N = 40, late N = 60 for trial-to-trial comparisons shown in Fig. 4. Comparison of trial-to-trial data was compared with a two-sided t-test with a p-value of 3.5e-6).

DISCUSSION

Mouse models are widely used to study the neural control of movement, motor disorders, muscle physiology and develop novel brain-computer interfaces and neurotechnologies. Despite the widespread use of mice in the health sciences, the only available biomechanical model of the mouse forelimb is based on educated guesses, which could lead to inaccurate kinematics and muscle activity predictions. We used high-detail anatomical reconstruction from large scale light sheet microscopy scans to develop the first physiological biomechanical model of the mouse forelimb in terms of musculoskeletal geometry and muscle architecture (Mathewson et al., 2012). Dissections to determine the musculoskeletal geometry would have been too challenging because of the small size of the mouse forelimb, especially in determining the attachment points of the minuscule tendons of the elbow. Other imaging techniques such as microCT would have likely also been adequate to produce sufficient soft tissue contrast for the reconstruction (Charles et al., 2016). We then used this biomechanical model with optimal control for usage in optimal control-based simulations to synthesize muscle coordination patterns that produce reaching movements that match experimental kinematics. Accurately predicting muscle activity is very challenging because of the infinite possible coordination patterns consistent with the tracked experimental kinematics and the high physiological variance in the patterns observed in real mice (i.e., for very similar kinematics, mice often use very different muscle activation strategies, some of which may be energetically costly, have high or low co-contraction, be robust to disturbances, etc.). Our optimal control cost function only has terms to encourage low energy (via the sum of muscle activations squared proxy) and producing kinematics consistent with experimental data. Therefore, we would not expect the optimal control predictions to closely match the experimental muscle activity on a reach-by-reach basis because of the high variability in the experimental muscle patterning data. Nevertheless, we found that the mean optimal control muscle activity predictions have strong resemblance with the mean empirical muscle activity (Fig. 3A). These results held for all three recorded muscles with EMG (biceps, triceps long head and triceps lateral head). As far as we know, this is the first work in any species, including humans, showing resemblance between synthesized and experimental muscle activity for three-dimensional reaching movements with a biomechanical model.

Neuroscience experiments are sometimes limited in scope by the difficulty of simultaneous recording of behavior, neurological signals, and, in some cases, muscle activity. Multisite muscle recordings are often limited to a handful of accessible sites, and this limitation is exacerbated in mice, where access to and implantation of many muscles is often infeasible. This model is meant to supplement experiments where knowledge of muscle activity patterning could bring insight about the nature of neural activity patterning. Scientists with behavioral data can extract an estimate of whole-forelimb muscle activity from the model given a set of kinematics over time. Tracking of mouse kinematics has become broadly accessible through the advent of pose-based tracking software like DeepLabCut, which was used in the present study to monitor limb position during reaching behaviors (Mathis et al., 2018). The conjunction of tracking and synthesis of full-limb muscle activations promises to expand research into behavioral control significantly.

There are several extensions to our biomechanical model and computational tools possible for future work. Our computational tools assume that no EMG is available during the experiments. If EMG is collected during the experiment, the optimal control problem can be solved to predict the muscle activity of muscles without EMG recordings while matching experimental EMG and kinematics data in tracking simulations (Dembia et al., 2021). It is also possible to change the cost function in the optimal control problem and produce predictive simulations that do not require any experimental data, including kinematics. The optimal control problem could then predict the reaching kinematics and muscle activity when there is a change in the task (e.g., a new pellet location) or to limb biomechanics (e.g., a weight placed on the forelimb). This study is focused on the ballistic phase of reaching movements. We did not model the grasping phase during the reach as we would have needed to include the muscles that control the wrist and fingers in the model and simulate interaction with the pellet. One discrepancy between our simulation and

the empirical reach is that mice, before starting their reach, were resting on a bar, which we did not simulate (and may impact the predicted muscle activity at the start of the ballistic phase).

Our simulations were evaluated with head-fixed mouse reaching. Using the biomechanical model in free-reaching mice may be less accurate because it has more significant scapula movements, which we assume to stay fixed in our model. In future work, researchers could either add a degree-of-freedom and a joint motor to allow translational movement of the scapula or incorporate the muscles that control the scapula as a free body in the biomechanical model (our scans available in supplementary materials should help delineate these muscles). The optimal control solutions produce open-loop muscle coordination patterns that are not responsive to noise or changing task or environmental constraints. It is however possible to develop closed-loop controllers to track the optimized trajectory or to develop feedback controllers with reinforcement learning, or introduce stochastic noise representing imprecise neural controls (e.g., Van Wouwe et al., 2022).

We make our computational tools freely available as open-source. Users of our computational tools should note that the optimal control predictions are expected to more closely resemble empirical muscle activity on a mean-basis rather than on a trial-by-trial basis and carry the assumption of closely matched kinematics. Furthermore, the predictions are expected to improve when mice have learned to perform the task well as opposed to when mice are still in the early stages of learning; nevertheless, the model predictions in the early stages of learning are still within one standard deviation of empirical results and represent a significant improvement over randomized guesses from the naturalistic EMG distribution. An exciting use case for our biomechanical model is to control it with artificial neural networks and relate the activity in these networks with empirical neural activity from system neuroscience laboratories (Aldarondo et al., 2024). Combining our computational tools and experimental data could lay the foundations for future studies elucidating the principles that drive the control of movement.

ACKNOWLEDGEMENTS

JIG designed the study, wrote the manuscript, assembled the model, and performed analysis. AGC performed imaging and prepared mice under the supervision of DH. SC trained mice, recorded electromyography, and provided datasets under the supervision of AP. JH helped design and conceptualize the study. MAB designed the study, wrote the manuscript, provided tools for analysis and supervised the study. We thank InWorks at CU Denver for imaging and segmentation. The behavioral study included in this work was supported by NIH grants (along w Simons Consortium): U24 NS126936 and R01 NS109237. JIG was supported by NLM grants 2T15LM009451-16 and 5T15LM009451-15.

REFERENCES

1. Al Borno, M., Vyas, S., Shenoy, K. V., & Delp, S. L. (2020). High-fidelity musculoskeletal modeling reveals that motor planning variability contributes to the speed-accuracy tradeoff. eLife, 9, e57021. https://doi.org/10.7554/eLife.57021
2. Aldarondo, D., Merel, J., Marshall, J. D., Hasenclever, L., Klibaite, U., Gellis, A., Tassa, Y., Wayne, G., Botvinick, M., & Ölveczky, B. P. (2024). A virtual rodent predicts the structure of neural activity across behaviours. Nature, 632(8025), 594–602. https://doi.org/10.1038/s41586-024-07633-4
3. Becker, M. I., Calame, D. J., Wrobel, J., & Person, A. L. (2020). Online control of reach accuracy in mice. Journal of Neurophysiology, 124(6), 1637–1655. https://doi.org/10.1152/jn.00324.2020
4. Becker, M. I., & Person, A. L. (2019). Cerebellar Control of Reach Kinematics for Endpoint Precision. Neuron, 103(2), 335-348.e5. https://doi.org/10.1016/j.neuron.2019.05.007
5. Blender Development Team. (2022). Blender (Version 3.2.2) [Computer software]. https://www.blender.org
6. Bollu, T., Whitehead, S. C., Prasad, N., Walker, J., Shyamkumar, N., Subramaniam, R., Kardon, B., Cohen, I., & Goldberg, J. H. (2019). Automated home cage training of mice in a hold-still center-out reach task. Journal of Neurophysiology, 121(2), 500–512. https://doi.org/10.1152/jn.00667.2018
7. Bonnefoi-Kyriacou, B., Legallet, E., Lee, R. G., & Trouche, E. (1998). Spatio-temporal and kinematic analysis of pointing movements performed by cerebellar patients with limb ataxia. Experimental Brain Research, 119(4), 460–466. https://doi.org/10.1007/s002210050361
8. Burgess, C. P., Lak, A., Steinmetz, N. A., Zatka-Haas, P., Bai Reddy, C., Jacobs, E. A. K., Linden, J. F., Paton, J. J., Ranson, A., Schröder, S., Soares, S., Wells, M. J., Wool, L. E., Harris, K. D., & Carandini, M. (2017). High-Yield Methods for Accurate Two-Alternative Visual Psychophysics in Head-Fixed Mice. Cell Reports, 20(10), 2513–2524. https://doi.org/10.1016/j.celrep.2017.08.047
9. Burkholder, T. J., Fingado, B., Baron, S., & Lieber, R. L. (1994). Relationship between muscle fiber types and sizes and muscle architectural properties in the mouse hindlimb. Journal of Morphology, 221(2), 177–190. https://doi.org/10.1002/jmor.1052210207
10. Calame, D. J., Becker, M. I., & Person, A. L. (2023). Cerebellar associative learning underlies skilled reach adaptation. Nature Neuroscience, 26(6), 1068–1079. https://doi.org/10.1038/s41593-023-01347-y
11. Charles, J. P., Cappellari, O., Spence, A. J., Hutchinson, J. R., & Wells, D. J. (2016). Musculoskeletal Geometry, Muscle Architecture and Functional Specialisations of the Mouse Hindlimb. PLOS ONE, 11(4), e0147669. https://doi.org/10.1371/journal.pone.0147669
12. Cheung, V. C. K., Turolla, A., Agostini, M., Silvoni, S., Bennis, C., Kasi, P., Paganoni, S., Bonato, P., & Bizzi, E. (2012). Muscle synergy patterns as physiological markers of motor cortical damage. Proceedings of the National Academy of Sciences, 109(36), 14652–14656. https://doi.org/10.1073/pnas.1212056109
13. Conner, J. M., Bohannon, A., Igarashi, M., Taniguchi, J., Baltar, N., & Azim, E. (2021). Modulation of tactile feedback for the execution of dexterous movement. Science, 374(6565), 316–323. https://doi.org/10.1126/science.abh1123
14. De Groote, F., Kinney, A. L., Rao, A. V., & Fregly, B. J. (2016). Evaluation of Direct Collocation Optimal Control Problem Formulations for Solving the Muscle Redundancy Problem. Annals of Biomedical Engineering, 44(10), 2922–2936. https://doi.org/10.1007/s10439-016-1591-9
15. Deisseroth, K., Feng, G., Majewska, A. K., Miesenböck, G., Ting, A., & Schnitzer, M. J. (2006). Next-Generation Optical Technologies for Illuminating Genetically Targeted Brain Circuits. The Journal of Neuroscience, 26(41), 10380–10386. https://doi.org/10.1523/JNEUROSCI.3863-06.2006
16. DeLaurier, A., Burton, N., Bennett, M., Baldock, R., Davidson, D., Mohun, T. J., & Logan, M. P. (2008). The Mouse Limb Anatomy Atlas: An interactive 3D tool for studying embryonic limb patterning. BMC Developmental Biology, 8(1), 83. https://doi.org/10.1186/1471-213X-8-83
17. Dembia, C. L., Bianco, N. A., Falisse, A., Hicks, J. L., & Delp, S. L. (2020). OpenSim Moco: Musculoskeletal optimal control. PLOS Computational Biology, 16(12), e1008493. https://doi.org/10.1371/journal.pcbi.1008493

18. Dogdas, B., Stout, D., Chatziioannou, A. F., & Leahy, R. M. (2007). Digimouse: A 3D whole body mouse atlas from CT and cryosection data. Physics in Medicine and Biology, 52(3), 577–587. https://doi.org/10.1088/0031-9155/52/3/003
19. Fedorov, A., Beichel, R., Kalpathy-Cramer, J., Finet, J., Fillion-Robin, J.-C., Pujol, S., Bauer, C., Jennings, D., Fennessy, F., Sonka, M., Buatti, J., Aylward, S., Miller, J. V., Pieper, S., & Kikinis, R. (2012). 3D Slicer as an image computing platform for the Quantitative Imaging Network. Magnetic Resonance Imaging, 30(9), 1323–1341. https://doi.org/10.1016/j.mri.2012.05.001
20. Fleischer, P., Abbasi, A., Fealy, A. W., Danielsen, N. P., Sandhu, R., Raj, P. R., & Gulati, T. (2023). Emergent Low-Frequency Activity in Cortico-Cerebellar Networks with Motor Skill Learning. Eneuro, 10(2), ENEURO.0011-23.2023. https://doi.org/10.1523/ENEURO.0011-23.2023
21. Galiñanes, G. L., Bonardi, C., & Huber, D. (2018). Directional Reaching for Water as a Cortex-Dependent Behavioral Framework for Mice. Cell Reports, 22(10), 2767–2783. https://doi.org/10.1016/j.celrep.2018.02.042
22. Habart, M., Lio, G., Soumier, A., Demily, C., & Sirigu, A. (2023). An optimized iDISCO+ protocol for tissue clearing and 3D analysis of oxytocin and vasopressin cell network in the developing mouse brain. STAR Protocols, 4(1), 101968. https://doi.org/10.1016/j.xpro.2022.101968
23. Harris, C. M., & Wolpert, D. M. (1998). Signal-dependent noise determines motor planning. Nature, 394(6695), 780–784. https://doi.org/10.1038/29528
24. Hebel, R., & Stromberg, M. W. (1986). Anatomy and embryology of the laboratory rat. BioMed Verl.
25. Iwaniuk, A. N., & Whishaw, I. Q. (2000). On the origin of skilled forelimb movements. Trends in Neurosciences, 23(8), 372–376. https://doi.org/10.1016/S0166-2236(00)01618-0
26. Kewley, A., Beesel, J., & Seth, A. (2024). OpenSim Creator (Version 0.5.12) [Computer software]. Zenodo. https://doi.org/10.5281/ZENODO.11086325
27. Khanna, P., Totten, D., Novik, L., Roberts, J., Morecraft, R. J., & Ganguly, K. (2021). Low-frequency stimulation enhances ensemble co-firing and dexterity after stroke. Cell, 184(4), 912-930.e20. https://doi.org/10.1016/j.cell.2021.01.023
28. Mathewson, M. A., Chapman, M. A., Hentzen, E. R., Fridén, J., & Lieber, R. L. (2012). Anatomical, architectural, and biochemical diversity of the murine forelimb muscles. Journal of Anatomy, 221(5), 443–451. https://doi.org/10.1111/j.1469-7580.2012.01559.x
29. Mathis, A., Mamidanna, P., Cury, K. M., Abe, T., Murthy, V. N., Mathis, M. W., & Bethge, M. (2018). DeepLabCut: Markerless pose estimation of user-defined body parts with deep learning. Nature Neuroscience, 21(9), 1281–1289. https://doi.org/10.1038/s41593-018-0209-y
30. Navarro, M., Ruberte, J., & Carretero, A. (2017). Myology. In Morphological Mouse Phenotyping (pp. 63–88). Elsevier. https://doi.org/10.1016/B978-0-12-812972-2.50004-0
31. Powell, P. L., Roy, R. R., Kanim, P., Bello, M. A., & Edgerton, V. R. (1984). Predictability of skeletal muscle tension from architectural determinations in guinea pig hindlimbs. Journal of Applied Physiology, 57(6), 1715–1721. https://doi.org/10.1152/jappl.1984.57.6.1715
32. Robbins, A., Tom, C. A. T. M. B., Cosman, M. N., Moursi, C., Shipp, L., Spencer, T. M., Brash, T., & Devlin, M. J. (2018). Low temperature decreases bone mass in mice: Implications for humans. American Journal of Physical Anthropology, 167(3), 557–568. https://doi.org/10.1002/ajpa.23684
33. Sauerbrei, B. A., Guo, J.-Z., Cohen, J. D., Mischiati, M., Guo, W., Kabra, M., Verma, N., Mensh, B., Branson, K., & Hantman, A. W. (2020). Cortical pattern generation during dexterous movement is input-driven. Nature, 577(7790), 386–391. https://doi.org/10.1038/s41586-019-1869-9
34. Serradj, N., Marino, F., Moreno-López, Y., Bernstein, A., Agger, S., Soliman, M., Sloan, A., & Hollis, E. (2023). Task-specific modulation of corticospinal neuron activity during motor learning in mice. Nature Communications, 14(1), 2708. https://doi.org/10.1038/s41467-023-38418-4
35. Seth, A., Hicks, J. L., Uchida, T. K., Habib, A., Dembia, C. L., Dunne, J. J., Ong, C. F., DeMers, M. S., Rajagopal, A., Millard, M., Hamner, S. R., Arnold, E. M., Yong, J. R., Lakshmikanth, S. K., Sherman, M. A., Ku, J. P., & Delp, S. L. (2018). OpenSim: Simulating musculoskeletal dynamics and neuromuscular

control to study human and animal movement. PLOS Computational Biology, 14(7), e1006223. https://doi.org/10.1371/journal.pcbi.1006223

36. Seth, A., Matias, R., Veloso, A. P., & Delp, S. L. (2016). A Biomechanical Model of the Scapulothoracic Joint to Accurately Capture Scapular Kinematics during Shoulder Movements. PLOS ONE, 11(1), e0141028. https://doi.org/10.1371/journal.pone.0141028
37. Tata Ramalingasetty, S., Danner, S. M., Arreguit, J., Markin, S. N., Rodarie, D., Kathe, C., Courtine, G., Rybak, I. A., & Ijspeert, A. J. (2021). A Whole-Body Musculoskeletal Model of the Mouse. IEEE Access, 9, 163861–163881. https://doi.org/10.1109/ACCESS.2021.3133078
38. Todorov, E., Erez, T., & Tassa, Y. (2012). MuJoCo: A physics engine for model-based control. 2012 IEEE/RSJ International Conference on Intelligent Robots and Systems, 5026–5033. https://doi.org/10.1109/IROS.2012.6386109
39. Uchida, T. K., Delp, S., & Delp, D. B. (2020a). Biomechanics of movement: The science of sports, robotics, and rehabilitation. The MIT Press.
40. Van Wouwe, T., Ting, L. H., & De Groote, F. (2022). An approximate stochastic optimal control framework to simulate nonlinear neuro-musculoskeletal models in the presence of noise. PLOS Computational Biology, 18(6), e1009338. https://doi.org/10.1371/journal.pcbi.1009338
41. Vissani, M., Palmisano, C., Volkmann, J., Pezzoli, G., Micera, S., Isaias, I. U., & Mazzoni, A. (2021). Impaired reach-to-grasp kinematics in parkinsonian patients relates to dopamine-dependent, subthalamic beta bursts. Npj Parkinson's Disease, 7(1), 53. https://doi.org/10.1038/s41531-021-00187-6
42. Voigt, F. F., Kirschenbaum, D., Platonova, E., Pagès, S., Campbell, R. A. A., Kastli, R., Schaettin, M., Egolf, L., Van Der Bourg, A., Bethge, P., Haenraets, K., Frézel, N., Topilko, T., Perin, P., Hillier, D., Hildebrand, S., Schueth, A., Roebroeck, A., Roska, B., … Helmchen, F. (2019). The mesoSPIM initiative: Open-source light-sheet microscopes for imaging cleared tissue. Nature Methods, 16(11), 1105–1108. https://doi.org/10.1038/s41592-019-0554-0
43. Wagner, M. J., Kim, T. H., Kadmon, J., Nguyen, N. D., Ganguli, S., Schnitzer, M. J., & Luo, L. (2019). Shared Cortex-Cerebellum Dynamics in the Execution and Learning of a Motor Task. Cell, 177(3), 669-682.e24. https://doi.org/10.1016/j.cell.2019.02.019
44. Yang, W., Kanodia, H., & Arber, S. (2023). Structural and functional map for forelimb movement phases between cortex and medulla. Cell, 186(1), 162-177.e18. https://doi.org/10.1016/j.cell.2022.12.009
45. Zia, M., Chung, B., Sober, S., & Bakir, M. S. (2020). Flexible Multielectrode Arrays With 2-D and 3-D Contacts for In~ Vivo Electromyography Recording. IEEE Transactions on Components, Packaging and Manufacturing Technology, 10(2), 197–202. https://doi.org/10.1109/TCPMT.2019.2963556

Table 1. Muscle origins and insertions.

Muscle Name	Origin Parent-Body	Origin Coordinates (m)	Insertion Parent-Body	Insertion Coordinates (m)
Anconeus	Humerus	[5.2e-3, 5e-4, 1.07e-2]	Ulna	[2.4e-3, -2e-4, 8.8e-3]
Anconeus, Short Head	Humerus	[3.6e-3, -9e-4, 9.1e-3]	Ulna	[3.8e-3, -6e-4, 8.3e-3]
Biceps, Long Head	Scapula	[8.5-3, 2.3e-2,1.2e-2]	Ulna	[2.1e-3, 4.9e-5, 8.8e-3]
Biceps, Short Head	Humerus	[9.1e-3, 1.5e-3,1.2e-2]	Ulna	[2.1e-3, 9.8e-5, 8.8e-3]
Brachialis, Proximal Head	Humerus	[2.3e-3, 5.9e-5, 8.8e-3]	Ulna	[2.2-3, 5.9e-5, 8.8e-3]
Brachialis, Distal Head	Humerus	[8.2e-3, 1.4e-3, 1.2e-2]	Ulna	[2.2-3, 5.9e-5, 8.8e-3]
Brachioradialis	Humerus	[4e-3, 6.5e-4, 9.1e-3]	Radius	[-3e-3, 1.3e-3, 1.2e-2]
Deltoid, Medial	Clavicle	[9.3e-3. 5e-4, 1.3e-2]	Humerus	[5.5e-3, 1.2e-3, 1.2e-2]
Deltoid, Posterior	Scapula	[8.7e-3, 1.2e-3, 1.2e-2]	Humerus	[5.9e-3, 1.5e-3, 1.1e-2]
Flexorcarpiradialis	Humerus	[3.4e-3, -9.3e-4, 9.2e-3]	Hand	[-4e-3, 1.6e-3, 1.2e-2]
Infraspinatus	Scapula	[1.1e-2, 1.3e-3, 1.2e-2]	Humerus	[8.3e-3, 1.6e-3, 1.2e-2]
Latissimus Dorsi, Caudal	Spine*	[1.8e-2, -3e-3, 1e-2]	Humerus	[5.5e-3, 1.7e-3, 1.1e-2]
Latissimus Dorsi, Rostral	Spine*	[1.5e-2, -7.1e-4, 1.3e-2]	Humerus	[5.9e-3, 1.5e-3, 1.1e-2]
Pectoralis Major, Anterior	Rib-cage*	[9.1e-3, -1.6e-3, 1.7e-2]	Humerus	[5.3e-3, 1.4e-3, 1.2e-2]
Pectoralis Major, Posterior	Rib-cage*	[1e-2, -3.1e-3, 1.5e-2]	Humerus	[5.5e-3, 1e-3, 1.2e-2]
Pectoralis Minor, Clavicular	Clavicle	[1.1e-2, -9.6e-4, 1.3e-2]	Humerus	[5.6e-3, 1.2e-3, 1.2e-2]
Pronator Teres	Humerus	[3.6e-3, -6.7e-4, 9.3e-3]	Radius	[8.8e-4, 1.2e-3, 1e-2]
Subscapularis	Scapula	[1.3e-2, 4e-4, 1.3e-2]	Humerus	[8.2e-3, 6.2e-4, 1.2e-2]
Triceps, Long Head	Scapula	[9.8e-3, 1.2e-3, 1.2e-2]	Ulna	[4.2e-3, -5.7e-4, 8e-3]
Triceps, Lateral Head	Humerus	[8.4e-3, 1.6e-3, 1.2e-2]	Ulna	[4.1-3, -4.5e-4, 8.3e-3]
Triceps, Medial Head	Humerus	[6.5e-3, 2.5e-4, 1.1e-2]	Ulna	[3.8e-3, -2.3e-4, 8.4e-3]

* Spinal and rib attachments made to Scapula fixed ground object.

Table 2. Muscle Parameters

Muscle Name	Max Isometric Force (N)	Optimal Fiber Length (m)	Pennation Angle (rad)	Tendon Slack Length (m)
Anconeus	0.023	0.003	0.1	0.0002
Anconeus, Short Head	0.02	0.0015	0.1	0.00015
Biceps, Long Head	0.093	0.0085	0.1	0.0002
Biceps, Short Head	0.018	0.005	0.1	0.0005
Brachialis, Proximal Head	0.066	0.007	0.1	0.0001
Brachialis, Distal Head	0.067	0.007	0.1	0.0001
Brachioradialis	0.02	0.007	0.1	0.0001
Deltoid, Medial	0.069	0.006	0.2	0.0002
Deltoid, Posterior	0.068	0.0035	0.2	0.0001
Flexorcarpiradialis	0.02	0.007	0.1	0.0001
Infraspinatus	0.065	0.003	0.2	0.0001
Latissimus Dorsi, Caudal	0.133	0.011	0.36	0.0005
Latissimus Dorsi, Rostral	0.1133	0.011	0.36	0.0005
Pectoralis Major, Anterior	0.233	0.008	0.3	0.0002
Pectoralis Major, Posterior	0.170	0.007	0.3	0.0005
Pectoralis Minor, Clavicular	0.033	0.0056	0.25	0.0002
Pronator Teres	0.02	0.003	0.1	0.0001
Subscapularis	0.34	0.005	0.2	0.0001
Triceps, Long Head	0.612	0.008	0.3	0.0007
Triceps, Lateral Head	0.125	0.007	0.17	0.0001
Triceps, Medial Head	0.16	0.004	0.2	0.0001